

Full Transport General Relativistic Radiation Magnetohydrodynamics for Nucleosynthesis in Collapsars

JONAH M. MILLER,^{1,2,3} TREVOR M. SPROUSE,^{4,5,6} CHRISTOPHER L. FRYER,^{7,8} BENJAMIN R. RYAN,^{1,2}
JOSHUA C. DOLENCE,^{1,2} MATTHEW R. MUMPOWER,^{6,8} AND REBECCA SURMAN⁵

¹*Computational Physics and Methods, Los Alamos National Laboratory, Los Alamos, NM, USA*

²*Center for Theoretical Astrophysics, Los Alamos National Laboratory, Los Alamos, NM, USA*

³*Center for Nonlinear Studies, Los Alamos National Laboratory, Los Alamos, NM, USA*

⁴*Los Alamos Center for Space and Earth Science Student Fellow*

⁵*Department of Physics, University of Notre Dame, Notre Dame, IN, USA*

⁶*Theoretical Division, Los Alamos National Laboratory, Los Alamos, NM 87545, USA*

⁷*Computational Physics and Methods, Los Alamos National Laboratory, Los Alamos, NM 87545, USA*

⁸*Center for Theoretical Astrophysics, Los Alamos National Laboratory, Los Alamos, NM 87545, USA*

Submitted to ApJ

ABSTRACT

We model a compact black hole-accretion disk system in the collapsar scenario with full transport, frequency dependent, general relativistic radiation magnetohydrodynamics. We examine whether or not winds from a collapsar disk can undergo rapid neutron capture (r-process) nucleosynthesis and significantly contribute to solar r-process abundances. We find the inclusion of accurate transport has significant effects on outflows, raising the electron fraction above $Y_e \sim 0.3$ and preventing third peak r-process material from being synthesized. We analyze the time-evolution of neutrino processes and electron fraction in the disk and present a simple one-dimensional model for the vertical structure that emerges. We compare our simulation to semi-analytic expectations and argue that accurate neutrino transport and realistic initial and boundary conditions are required to capture the dynamics and nucleosynthetic outcome of a collapsar.

1. INTRODUCTION

When a massive, rapidly rotating star collapses, it may fail to explode. Post-bounce, the proto-neutron star collapses and forms a black hole. In this scenario, stellar material eventually circularizes and accretes onto the central black hole. Woosley (1993) coined this a “failed” supernova, with “failed” in quotes, since an accretion-driven jet may indeed cause an explosion. MacFadyen & Woosley (1999) coined this the collapsar scenario, and this system a collapsar. These events are commonly invoked as the sources of long gamma ray bursts (GRBs), and observational evidence is consistent with this hypothesis (Woosley & Bloom 2006; Ghirlanda et al. 2009; Hjorth & Bloom 2012).

The dynamics of stellar collapse and the formation of a GRB engine has thus been studied extensively, see Woosley (1993); MacFadyen & Woosley (1999); Mac-

Fadyen et al. (2001); Proga et al. (2003); Heger et al. (2003); Mizuno et al. (2004); Fujimoto et al. (2006); Nagataki et al. (2007); Rockefeller et al. (2006); Uzdensky & MacFadyen (2007); Morsony et al. (2007); Bucciantini et al. (2008); Lazzati et al. (2008); Kumar et al. (2008); Nagakura et al. (2011); Taylor et al. (2011); Ott et al. (2011); Lindner et al. (2012); López-Cámara et al. (2013); Batta & Lee (2014); Liu et al. (2017) and references therein. Recently, attention has been devoted to the related case where a rapidly rotating star collapses to a protoneutron star and black hole formation is either delayed or does not happen at all (Thompson et al. 2004; Metzger et al. 2008; Winteler et al. 2012; Mösta et al. 2014, 2018; Halevi & Mösta 2018).

MacFadyen & Woosley (1999) realized that the dynamics of collapsar disks are similar to other neutron-rich compact accretion flows such as those formed by a binary neutron star merger. This implies that collapsar disks may be a proposed site of rapid neutron capture (r-process) nucleosynthesis, the mechanism by which the heaviest elements in our universe are formed

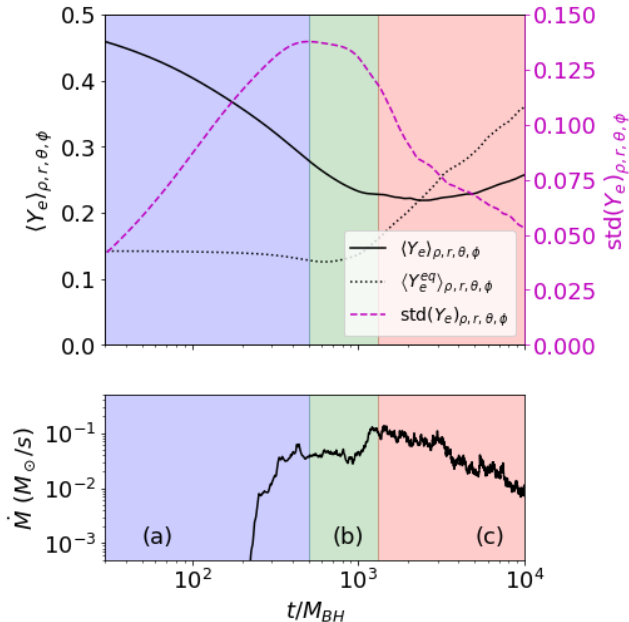


Figure 1. Density-weighted mean and standard deviation of electron fraction Y_e (top) and accretion rate \dot{M} (bottom) as a function of time. The dotted black line shows the density-weighted mean *equilibrium* value of Y_e as opposed to the one realized in the simulation. The evolution of the disk can be roughly broken into three phases, (a), (b), and (c), described in the text.

(Howard et al. 1972; Lattimer & Schramm 1976; Lattimer et al. 1977; Blinnikov et al. 1984; Kohri et al. 2005; Côté et al. 2018).¹ Nucleosynthesis in rapidly rotating core collapse—with and without black hole formation—has been explored by several groups (Popham et al. 1999; Di Matteo et al. 2002; Surman & McLaughlin 2004; McLaughlin & Surman 2005; Surman et al. 2006; Thompson et al. 2004; Rockefeller et al. 2008; Metzger et al. 2008; Winteler et al. 2012; Mösta et al. 2014, 2018; Halevi & Mösta 2018).

At low entropies, electron fraction becomes the deciding factor in the r-process. For r-process elements to be synthesized, the central engine must produce outflows with low electron fraction Y_e . A robust r-process typically requires $Y_e \lesssim 0.25$. Early semi-analytic work found that collapsar outflows are insufficiently neutron-rich (Popham et al. 1999; Di Matteo et al. 2002; Surman & McLaughlin 2004; McLaughlin & Surman 2005; Surman et al. 2006). In the magnetar case, where no black hole formation occurs, three-dimensional simulations show that non-axisymmetric effects can make it difficult to eject a sufficient amount of low Y_e material.

Thus whether or not a magnetar can eject heavy elements depends on factors that control the symmetry of the problem, such as magnetic field strength and how quickly the jet develops (Mösta et al. 2014, 2018; Halevi & Mösta 2018).

One proposed mechanism for producing massive, neutron-rich outflows is that material may be entrained in a low-density relativistic jet (Fujimoto et al. 2007; Ono et al. 2012; Nakamura et al. 2015; Soker & Gilkis 2017; Hayakawa & Maeda 2018). One promising aspect of this approach is that material entrained in the jet may have high entropy, which means that it may undergo rapid neutron capture even with higher Y_e . Most of these works assume axisymmetry, which means they do not properly account for the non-axisymmetric kink instability (Mösta et al. 2014) and suffer from the anti-dynamo theorem (Cowling 1933, 1957). Another issue is that if a jet is loaded with too much material, it cannot reach large Lorentz factors, meaning there is a tension between producing a robust jet and producing a sufficient amount of r-process material. It remains to be seen whether this mechanism holds up for realistic three-dimensional models and whether or not it can provide a meaningful contribution to abundances of r-process elements in the universe.

Recently Siegel et al. (2019) argued that collapsar fallback and subsequent accretion onto the central black hole can be approximately modeled by a magnetohydrodynamically driven accretion disk. They performed a suite of three-dimensional magnetohydrodynamic simulations, each corresponding to a different accretion rate, and thus a different phase of the core-collapse fallback. They find that the outflow from their simulation with the highest accretion rate is neutron-rich and they use this result to argue that collapsars are a primary source of r-process elements in the universe. In addition to the nucleosynthetic implications, Siegel et al. (2019) make an observable prediction about long GRBs. Assuming a long GRB is driven by a collapsar, the radioactive decay of r-process elements from the outflow implies an infra-red excess in the afterglow of such an event.

Siegel et al. (2019) modeled neutrino radiation with a leakage scheme first described in Siegel & Metzger (2018) and based on a long lineage (Bruenn 1985; Ruffert et al. 1997; Galeazzi et al. 2013; Radice et al. 2016). However, neutrino transport can have significant effects on the electron fraction and nucleosynthesis in compact accretion flows (Miller et al. 2019b). We therefore wish to see how improved transport effects the collapsar scenario. We model the highest accretion rate and thus densest, highest temperature, lowest electron fraction and most nucleosynthetically optimistic disk from Siegel

¹ For recent review of the r-process, see Cowan et al. (2019).

et al. (2019) with full frequency dependent general relativistic neutrino radiation magnetohydrodynamics. We then perform r-process nucleosynthesis calculations on the resulting outflow in post-processing.

We find that neutrino transport has significant effects on the disk outflow. In particular, although rapid neutron capture occurs, Y_e is not low enough in the outflow to produce third-peak r-process material. We also use our model to explore the hypothesis that a compact accretion disk is a sufficiently descriptive surrogate for a full collapsar. Although we are unable to make strong claims on the validity of using a single disk as a proxy for a collapsar, we argue that models with better initial and boundary conditions will continue to lack 3rd-peak r-process elements. However, further work is required to more deeply understand the system as a whole.

In section 2, we describe the physical system we simulate. In section 3, we describe our numerical method and

discuss resolution requirements. In section 4, we present results from our simulation, including steady-state disk properties, outflow statistics, and nucleosynthetic yield. In section 5, we examine systematic effects in our simulation. We discuss the importance of full neutrino transport and neutrino absorption in achieving our steady-state disk and outflow properties and we comment on the influence of the initial and boundary conditions and discuss the prospect of outflow material escaping the star. Finally, in section 6, we summarize our results and discuss some implications of our work.

2. THE MODEL

We solve the equations of general relativistic ideal magnetohydrodynamics (MHD)²

$$\partial_t (\sqrt{-g}\rho u^t) + \partial_i (\sqrt{-g}\rho u^i) = 0 \quad (1)$$

$$\partial_t [\sqrt{-g} (T^t_\nu + \rho u^t \delta^t_\nu)] + \partial_i [\sqrt{-g} (T^i_\nu + \rho u^i \delta^i_\nu)] = \sqrt{-g} (T^\kappa_\lambda \Gamma^\lambda_{\nu\kappa} + G_\nu) \quad \forall \nu = 0, 1, 2, 3 \quad (2)$$

$$\partial_t (\sqrt{-g} B^i) + \partial_j [\sqrt{-g} (b^j u^i - b^i u^j)] = 0 \quad \forall i = 1, 2, 3 \quad (3)$$

$$\partial_t (\sqrt{-g}\rho Y_e u^t) + \partial_i (\sqrt{-g}\rho Y_e u^i) = \sqrt{-g} G_{Y_e} \quad (4)$$

where the energy-momentum tensor T^μ_ν is assumed to be

$$T^\mu_\nu = (\rho + u + P + b^2) u^\mu u_\nu + \left(P + \frac{1}{2} b^2 \right) \delta^\mu_\nu - b^\mu b_\nu \quad (5)$$

for metric $g_{\mu\nu}$, rest energy ρ , fluid four-velocity u^μ , internal energy density u , pressure P , and Christoffel connection $\Gamma^\alpha_{\beta\gamma}$. (Here and in the remainder of the text, unless otherwise specified, we set $G = c = 1$.)

Equation (1) represents conservation of baryon number. Equation (2) represents conservation of energy-momentum, subject to the radiation four-force G_ν . Equation (3) describes the evolution of magnetic fields, where

$$B^i = {}^* F^{it} \quad (6)$$

comprise the magnetic field components of the Maxwell tensor $F_{\mu\nu}$ and b^μ is the magnetic field four-vector

$${}^* F^{\mu\nu} = b^\mu u^\nu - b^\nu u^\mu. \quad (7)$$

Equation (4) describes the conservation of lepton number. G_{Y_e} is a source term describing the rate at which lepton density is transferred between the fluid and the radiation field.

We close our system with the SFHo equation of state, tabulated in the Stellar Collapse format (O'Connor & Ott 2010a,b) and described in Steiner et al. (2013). An equation of state relates the pressure P and specific internal energy ε to the density ρ , temperature T , and electron fraction Y_e :

$$P = P(\rho, T, Y_e) \quad (8)$$

$$\varepsilon = \varepsilon(\rho, T, Y_e). \quad (9)$$

We evolve ρ , $u = \rho\varepsilon$, and Y_e , but not T or P . So at a given time, we find T by inverting equation (9) before plugging it into equation (8) to find P .

We approximate our neutrinos as massless such that they obey the standard radiative transfer equation

$$\frac{D}{d\lambda} \left(\frac{h^3 I_{\epsilon,f}}{\epsilon^3} \right) = \left(\frac{h^2 \eta_{\epsilon,f}}{\epsilon^2} \right) - \left(\frac{\epsilon \chi_{\epsilon,f}}{h} \right) \left(\frac{h^3 I_{\epsilon,f}}{\epsilon^3} \right), \quad (10)$$

where $D/d\lambda$ is the derivative along a neutrino trajectory in phase space, $I_{\epsilon,f}$ is the specific intensity of the

² Unless otherwise noted, we assume Greek indices range over spacetime, from 0 to 3, and Latin indices range over space, from 1 to 3.

| Type | Processes | Charged/Neutral | Corrections/Approximations |
|-------------------------------|--|-------------------|--|
| Electron Capture on Protons | $\nu_e + n \leftrightarrow e^- + p$ $\nu_\mu + n \leftrightarrow \mu^- + p$ | Charged | Blocking/Stimulated Abs. Weak Magnetism Recoil |
| Positron Capture on Neutrons | $\bar{\nu}_e + p \leftrightarrow e^+ + n$ $\bar{\nu}_\mu + p \leftrightarrow \mu^+ + n$ | Charged | Blocking/Stimulated Abs. Weak Magnetism Recoil |
| Abs./Emis. on Ions | $\nu_e A \leftrightarrow A' e^-$ | Charged | Blocking/Stimulated Abs. Recoil |
| Electron Capture on Ions | $e^- + A \leftrightarrow A' + \nu_e$ | Charged | Blocking/Stimulated Abs. Recoil |
| $e^+ - e^-$ Annihilation | $e^+ e^- \leftrightarrow \nu_i \bar{\nu}_i$ | Charged + Neutral | single- ν Blocking Recoil |
| n_i - n_i Brehmsstrahlung | $n_i^1 + n_i^2 \rightarrow n_i^3 + n_i^4 + \nu_i \bar{\nu}_i$ | Neutral | single- ν Blocking Recoil |

Table 1. Emission and Absorption Processes used in *ν bhlight*.

NOTE—The symbols in the processes are as follows: n is a neutron, p a proton, e^- an electron, e^+ a proton, μ^- a muon, μ^+ an antimuon, and n_i an arbitrary nucleon. ν_i is an arbitrary neutrino. ν_e is an electron neutrino, and $\bar{\nu}_e$ is an electron antineutrino. We describe the corrections and approximations used below, as tabulated in Skinner et al. (2019) and provided to us in Burrows (2018). Blocking and stimulated absorption are related to the Fermi-Dirac nature of neutrinos. Weak magnetism is related to the extended quark structure of nucleons. Recoil is the kinematic recoil. Single- ν blocking is a Kirchhoff’s law based approximation of blocking that becomes exact for processes that involve only a single neutrino. The details of these interactions are summarized in Burrows et al. (2006). This table was first presented in its current form in Miller et al. (2019a).

neutrino field of flavor $f \in \{\nu_e, \bar{\nu}_e, \nu_x\}$,

$$\chi_{\epsilon,f} = \alpha_{\epsilon,f} + \sigma_{\epsilon,f}^a \quad (11)$$

is the extinction coefficient that combines absorption coefficient $\alpha_{\epsilon,f}$ and scattering extinction $\sigma_{\epsilon,f}^a$ for scattering interaction a and

$$\eta_{\epsilon,f} = j_{\epsilon,f} + \eta_{\epsilon,f}^s(I_{\epsilon,f}) \quad (12)$$

is the emissivity combining fluid emissivity $j_{\epsilon,f}$ and emission due to scattering from $\eta_{\epsilon,f}^s$. Here h is Planck’s constant, ϵ is the energy of a neutrino with wavevector k^μ as measured by an observer traveling along a timelike Killing vector η^μ .

Neutrinos can interact with matter via emission, absorption, or scattering. The latter does not change electron fraction Y_e , while the former two do. For emission and absorption, we use the charged and neutral current interactions as tabulated in Skinner et al. (2019) and described in Burrows et al. (2006). We summarize these interactions in Table 1, which was first presented in Miller et al. (2019a). We treat inelastic scattering off of electrons, nucleons, and heavy nuclei. Our scattering implementation uses a biasing technique to ensure all processes are well sampled, as described in Miller et al. (2019a).

3. METHODS

We simulate a disk of accretion rate $\dot{M} \approx 10^{-1} M_\odot/s$ in a stationary Kerr black hole spacetime (Kerr 1963) for a black hole of mass $M_{\text{BH}} = 3M_\odot$ and dimensionless spin $a = 0.8$, corresponding to the most nucleosynthetically optimistic (and highest \dot{M}) case presented in Siegel et al. (2019). To form the accretion disk, we begin with a torus in hydrostatic equilibrium (Fishbone & Moncrief 1976) of constant specific angular momentum, constant entropy of $s = 8k_b/\text{baryon}$, constant electron fraction $Y_e = 0.5$, and total mass of $M_d = 0.02M_\odot$. These conditions imply our torus has an inner radius of $5.5 GM_{\text{BH}}/c^2$ and a radius of peak pressure of $12.525 GM_{\text{BH}}/c^2$. Our torus starts with a single poloidal magnetic field loop with a minimum ratio of gas to magnetic pressure β of 100. As the system evolves, the magnetorotational instability (MRI, Balbus & Hawley 1991) self-consistently drives the disk to a turbulent state, which provides the turbulent viscosity necessary for the disk to accrete (Shakura & Sunyaev 1973).

We use our code *ν bhlight* (Miller et al. 2019a), based on *bhlight* (Ryan et al. 2015), which uses operator splitting to couple GRMHD via finite volume methods with constrained transport (Gammie et al. 2003) to neutrino transport via Monte Carlo methods (Dolence et al. 2009). We use a radially logarithmic, quasi-spherical grid in horizon penetrating coordinates, as first presented in Gammie et al. (2003) with $N_r \times N_\theta \times N_\phi = 192 \times 168 \times 66$

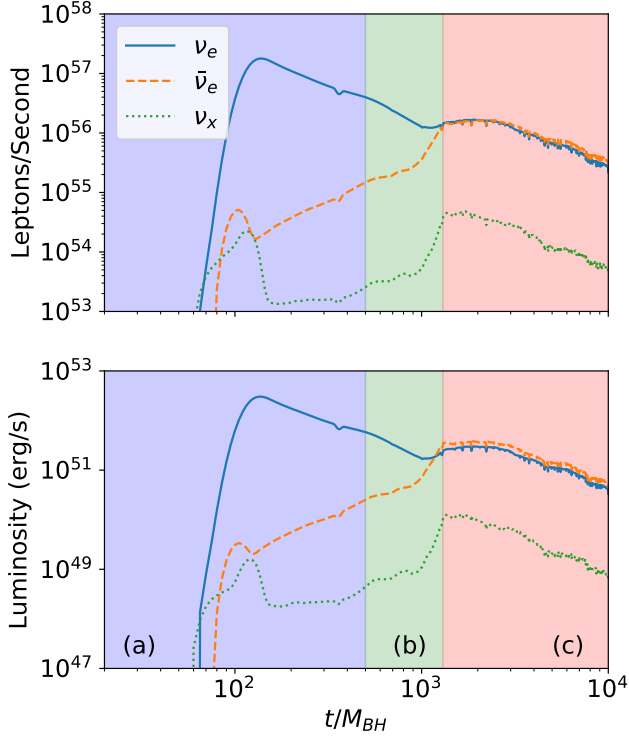


Figure 2. Luminosity (bottom) and particles per second (top) for electron neutrinos, electron antineutrinos, and heavy neutrinos measured at infinity as functions of time. The phases identified in Figure 1 are shown. The luminosity for heavy neutrinos is universally orders of magnitude lower than for the electron neutrinos and their antiparticles. At early times, the luminosity for electron neutrinos is much higher than for electron anti-neutrinos, consistent with rapid deleptonization. At late times, electron neutrinos and their antiparticles are roughly in balance, with a slight excess in anti-neutrinos, consistent with a slow re-leptonization process.

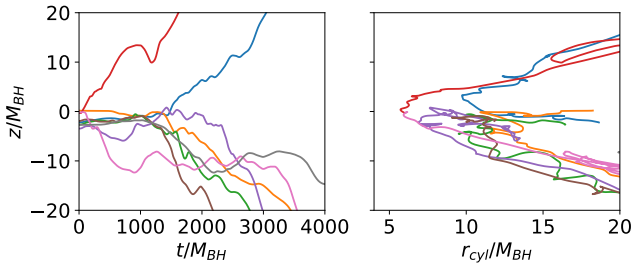


Figure 3. A random selection of traces that vary in latitude within the disk. We show height z as a function of time (left) and cylindrical radius $r_{\text{cyl}} = \sqrt{x^2 + y^2}$ (right). Notice that tracer paths are not linear. Rather, an individual fluid packet appears to random walk through space.

grid points with approximately 3×10^7 Monte Carlo packets. Although our code is Eulerian, we track Lagrangian fluid packets with approximately 1.5×10^6

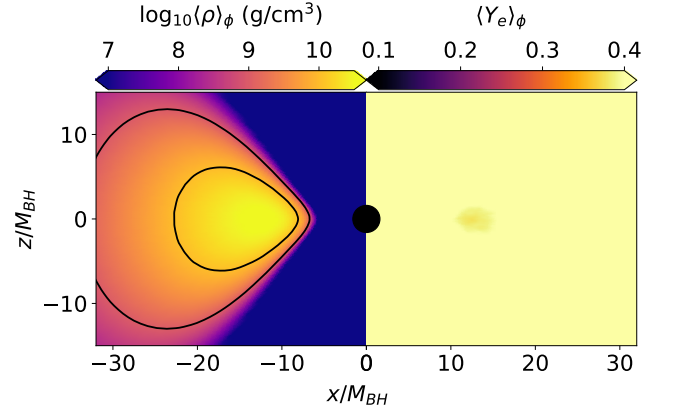


Figure 4. Density ρ (left) and electron fraction Y_e (right) near the initial time, at $t = 25GM_{\text{BH}}/c^3$ or ≈ 0.3 ms. Contours are for $\rho = 10^9$ and 10^{10} g/cm³. At this time, Y_e is almost universally 0.5 and deleptonization is beginning. Quantities are averaged over azimuthal angle ϕ .

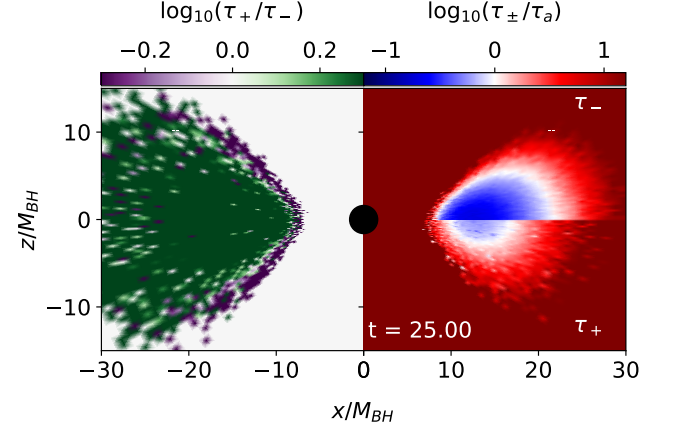


Figure 5. Comparison of relevant time scales for processes that can change Y_e : an increase due to radiation τ_+ , a decrease due to radiation τ_- and change due to turbulent flow τ_a . Plotted are: ratio of τ_+/τ_- (left), ratio of τ_-/τ_a (top right), and ratio of τ_+/τ_a (bottom right), near the initial time, at $t = 25GM_{\text{BH}}/c^3$ or ≈ 0.3 ms and averaged over azimuthal angle ϕ .

“tracer particles,” of which approximately 5×10^5 become gravitationally unbound. Following [Bovard & Rezzolla \(2017\)](#), our tracer particles are initialized within the disk so that they uniformly sample disk material by volume. For more information on our code implementation and verification, see [Miller et al. \(2019a\)](#). For a first application of $\nu\text{bhlight}$ in the context of neutron star mergers, see [Miller et al. \(2019b\)](#).

We run our simulation for approximately $10^4 GM_{\text{BH}}/c^3$, or 148 ms, which allows us to observe the disk in a quasistationary turbulent state. In the collapsar paradigm, the disk is fed by circularized

fallback from the progenitor star as it undergoes gravitational collapse. The initial phase of our simulation, where we relax an equilibrium torus, comprises an unphysical transient, and we wish to ignore material driven off the disk in this transient phase. We therefore neglect outflow which reaches a surface of $r = 250GM_{\text{BH}}/c^2$ within the first half of the simulation, $t < 5 \times 10^3 GM_{\text{BH}}/c^3$. Note that this corresponds to material ejected from the disk at much earlier times. We experimented with the amount of time we neglect and found that it does not significantly change the results presented below.

An accurate magnetohydrodynamic model of turbulent viscosity requires capturing the MRI (Balbus & Hawley 1991). Following Sano et al. (2004), we define a quality factor

$$Q_{\text{mri}}^{(\theta)} = \frac{2\pi b^{(\theta)}}{\Delta x^{(\theta)} \sqrt{w + b^2 \Omega}}, \quad (13)$$

for the MRI to be the number of grid points per minimum unstable MRI wavelength inside the disk. Here $b^{(\theta)}$ is the θ -component of the magnetic field four-vector, $\Delta x^{(\theta)}$ is grid spacing in the θ direction, w is the enthalpy of the fluid, Ω is the angular velocity of the flow, and $b^2 = b^\mu b_\mu$ is total magnetic field strength. To resolve the MRI, one needs at least ten grid points per smallest unstable MRI wavelength (Hawley et al. 2013). Our measurements of our disk satisfy this requirement, with $Q_{\text{mri}}^{(\theta)} \geq 10$ within the disk for all times.

Our simulation is not only magnetohydrodynamic, but radiation magnetohydrodynamic. Therefore, it is important also to ensure we are using a sufficient number of Monte Carlo packets to capture the relevant interactions between the gas and radiation field. Following Miller et al. (2019b), we define the Monte Carlo quality factor

$$Q_{\text{rad}} = \min_{r,\theta,\phi} \left(\frac{\partial N}{\partial t} \frac{u}{J} \right), \quad (14)$$

minimized over the simulation domain. N is the number of emitted Monte Carlo packets, u is gas internal energy density by volume, and J is the total frequency and angle integrated neutrino emissivity. Q_{rad} roughly encodes how well resolved the radiation field is, with $Q_{\text{rad}} = 10$ a marginal value. In our simulation, we find $Q_{\text{rad}} \gtrsim 100$ for all time.

4. RESULTS

4.1. Time Evolution and the Different Phases of Accretion

The bottom pane of Figure 1 shows the time evolution of the accretion rate of the disk. The accretion rate matches the standard time profile for MRI-powered

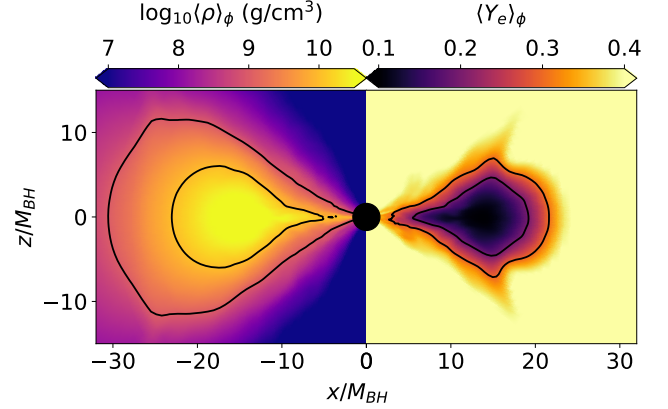


Figure 6. Same as Figure 4 but at $t = 500GM_{\text{BH}}/c^3$ or ≈ 7 ms.

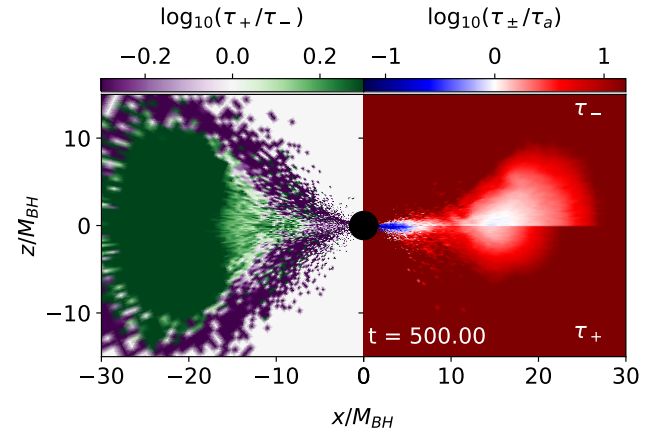


Figure 7. Same as Figure 5 but at $t = 500GM_{\text{BH}}/c^3$ or ≈ 7 ms.

disks with compact torus initial conditions (Shiokawa et al. 2011; Porth et al. 2019). The maximum accretion rate achieved for this realization is approximately $10^{-1} M_{\odot}/s$, which eventually undergoes power-law decay. This power law is well understood as an artifact of disks formed from a finite reservoir of material. In Nature, the disk is fed by fallback from the core-collapse event and thus the accretion rate will look different. In the top pane, we plot the density-weighted mean

$$\langle Y_e \rangle_{\rho,r,\theta,\phi} = \frac{\int_{\Omega} \sqrt{-g} dx^3 \rho Y_e}{\int_{\Omega} \sqrt{-g} dx^3 \rho}, \quad (15)$$

and standard deviation

$$\text{std}(Y_e)_{\rho,r,\theta,\phi} = \left[\frac{\int_{\Omega} \sqrt{-g} dx^3 \rho (Y_e - \langle Y_e \rangle_{\rho,r,\theta,\phi})^2}{\int_{\Omega} \sqrt{-g} dx^3 \rho} \right]^{1/2} \quad (16)$$

of the electron fraction Y_e as functions of time, where

$$\int_{\Omega} \sqrt{-g} dx^3$$

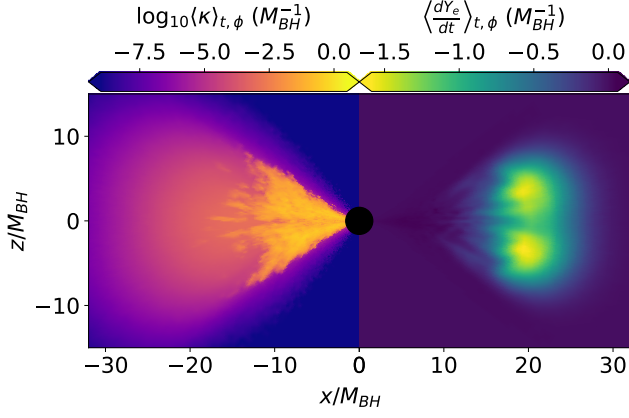


Figure 8. Neutrino opacity (left) and Lagrangian derivative of electron fraction in disk material (right). Opacity is integrated over frequency and flavor, weighted by the neutrino spectrum realized in the simulation. Both quantities are averaged over azimuthal angle ϕ and time in the early transient phase, from roughly 5 ms to 20 ms.

represents an integral over the whole domain with appropriate measure.

The accretion rate, together with the evolution of the electron fraction, suggest three phases, which will be described in more detail below:

- (a) As the initial torus disrupts and accretion flow is established, the disk rapidly deleptonizes. As a consequence, the mean electron fraction drops dramatically, while the standard deviation rises. This phase lasts for $t \lesssim 500 M_{\text{BH}}$ or $t \lesssim 7$ ms. We call this phase the *initial transient* phase.
- (b) After accretion begins, the disk enters a short transition period before establishing a quasi-stationary flow. We call this phase the *transition* phase, which roughly lasts for $500 M_{\text{BH}} \lesssim t \lesssim 1500 M_{\text{BH}}$ or $7 \text{ ms} \lesssim t \lesssim 22 \text{ ms}$.
- (c) In the quasi-stationary state, the accretion rate slowly drops as a power law. As the accretion rate drops, the electron fraction slowly rises and the standard deviation slowly drops. We call this the *steady-state* or *quasi-stationary* phase, which lasts for $t \gtrsim 1500 M_{\text{BH}} \approx 22 \text{ ms}$.

We emphasize that only phase (c) is representative of a collapsar in Nature. Phases (a) and (b) are unphysical transients that emerge from the initial conditions. Nevertheless, a good understanding of these transients is necessary for a complete picture of the structure in the disk in phase (c).

The bottom pane of Figure 2 shows the luminosity measured at infinity of electron neutrinos ν_e , electron

antineutrinos $\bar{\nu}_e$, and all other neutrino species, grouped together as “heavy neutrinos” or ν_x . The top pane shows the raw number of physical particles per second. The luminosity for heavy neutrinos is universally orders of magnitude lower than for the electron neutrinos and their antiparticles. The evolution of the luminosity is consistent with phases (a), (b), and (c). At early times, the luminosity for electron neutrinos is much higher than for electron anti-neutrinos, consistent with rapid deleptonization. At late times, electron neutrinos and their antiparticles are roughly in balance, with a slight excess in anti-neutrinos, consistent with a slow re-leptonization process.

4.2. Weak Equilibrium

When the probability of Y_e increasing in packet of material is in balance with the probability of Y_e decreasing, material is said to be in *weak equilibrium*. The classic example of weak equilibrium is β -equilibrium in a cold neutron star, where the probability of β -decay

$$n \rightarrow p + e + \bar{\nu}_e \quad (17)$$

is in balance with inverse β -decay

$$e + p \rightarrow n + \nu_e. \quad (18)$$

See, e.g., [Shapiro & Teukolsky \(2008\)](#) for a detailed discussion. For finite temperature systems out of equilibrium, such as the disk discussed here, β -decay is too slow to be dynamically relevant. Rather, the charged-current processes in table 1 determine the equilibrium ([Freedman 1974](#)).

For a given density ρ and temperature T , we can calculate the weak equilibrium electron fraction Y_e^{eq} such that these processes are in balance.³ The dotted black line in the top pane of Figure 1 shows the density-weighted mean value of Y_e^{eq} . Weak equilibrium is an extremely strong assumption, not realized in the simulation. However it provides a useful limiting case.

Throughout the accretion history, the disk is out of equilibrium and neutrino processes drive it towards equilibrium. This equilibrium is a moving target, as Y_e^{eq} at a given point in the disk changes as the conditions in the disk change with the accretion rate, and is not achieved during the lifetime of the simulation. Y_e begins far above the equilibrium value, which drives the rapid deleptonization of phase (a). As the accretion rate falls,

³ This calculation can be done in post-processing using the tabulated neutrino emissivities and opacities used by the code. For the purposes of Y_e^{eq} , and only Y_e^{eq} , we assume a radiation field in equilibrium with the gas.

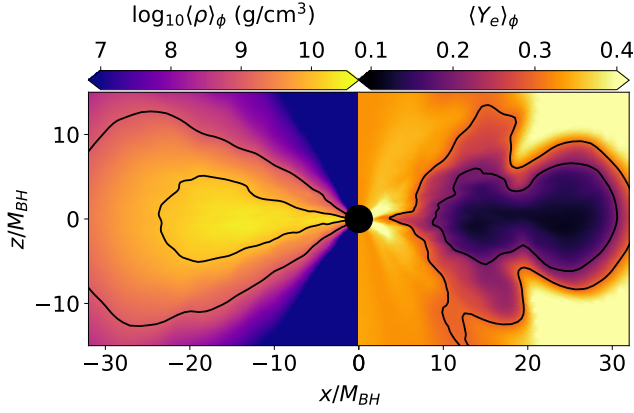


Figure 9. Same as Figure 4 but at $t = 1500 GM_{\text{BH}}/c^3$, or ≈ 22 ms.

the equilibrium electron fraction Y_e^{eq} rises, which in turn drives the late-time re-leptonization of the disk in phase (c).

4.3. Relevant Time Scales

Before we describe phases (a), (b), and (c) in more detail, we introduce several concepts we will make use of later. In particular, we are most interested in how electron fraction Y_e is set within the disk. There are essentially three relevant time scales. The first two are

$$\tau_{\pm} = \frac{\rho Y_e}{G_{Y_e}^{\pm}} \quad (19)$$

where $G_{Y_e}^{\pm}$ is the right-hand-side contribution to equation (4) that increases (for +) or decreases (for -) Y_e due to neutrino emission and absorption. Expressed more succinctly,

$$G_{Y_e} = G_{Y_e}^+ - G_{Y_e}^-. \quad (20)$$

We calculate this in-line within `νbhlight` by tracking the rate of Monte Carlo particles of each species emitted or absorbed. For more details see section 3 and equation 36 in Miller et al. (2019a).

The third time scale is set by the rate at which electron fraction is changed by advection and mixing. In other words, how long it takes for a fluid packet with a given Y_e to be advected with the flow to another location within the disk. As will be described in sections 4.8 and 4.10, the electron fraction in the disk is essentially a function of latitude $|90^\circ - \theta|$. Therefore, we focus on advection in the θ direction. Extracting this time scale is complicated by the fact that flow of material through the disk is not laminar. Indeed, MRI-driven turbulence is the dominant momentum transport mechanism in the disk (Balbus & Hawley 1991; Shakura & Sunyaev 1973).

Figure 3 shows how this fact influences the trajectories of individual Lagrangian fluid packets. We plot a random

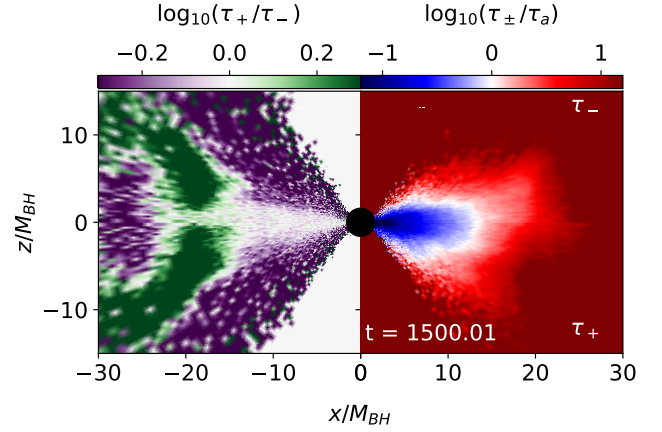


Figure 10. Same as Figure 5 but at $t = 1500 GM_{\text{BH}}/c^3$ or ≈ 22 ms.

selection of tracer particles, which are advected with the flow, that vary in latitude within the disk and eventually become gravitationally unbound. The left column shows height z as a function of time, while the right column shows it as a function of cylindrical radius

$$r_{\text{cyl}} = \sqrt{x^2 + y^2}. \quad (21)$$

Notice that tracer paths are not linear. Rather tracers, and thus Lagrangian fluid packets, “random walk” through the space. Note that the paths in Figure 3 project out the azimuthal flow. Thus the random walk includes the meandering visible in the figure and a turbulent orbit in the azimuthal direction.

To capture this idea, we introduce the spherically averaged, density and Y_e weighted, *advection velocity*

$$\langle v_a \rangle_{\rho, Y_e, \theta, \phi}(t, r) = \frac{\int_{S^2} \sqrt{-g} d^2 x \rho Y_e u^2}{\int_{S^2} \sqrt{-g} d^2 x \rho Y_e}, \quad (22)$$

where u^2 is the component of the four-velocity in the θ direction and

$$\int_{S^2} \sqrt{-g} d^2 x$$

is an integral over a thin spherical shell with appropriate measure. The integrand in the numerator of equation (22) is the flux in the equation for the conservation of lepton number (4), while the integrand in the denominator is general relativistically conserved lepton number in the same equation. Equation (22) thus tells us the rate that *leptons*, as opposed *baryons* change their angle θ .

To transform this into a time scale, we need a characteristic length scale. We follow Shiokawa et al. (2011) and calculate the *scale angle* of the disk as a function of radius and time:

$$\theta_d(t, r) = \sqrt{\frac{\int_{S^2} \sqrt{-g} d^2 x \rho \theta^2}{\int_{S^2} \sqrt{-g} d^2 x \rho}} \quad (23)$$

and the *scale height*

$$H(t, r) = r \tan(\theta_d(t, r)). \quad (24)$$

Then we define the *average advection time*

$$\tau_a(r) = \frac{1}{t_f - t_i} \int_{t_i}^{t_f} dt \frac{\theta_d}{\langle v_a \rangle_{\rho, Y_e, \theta, \phi}}, \quad (25)$$

where we have introduced a time-average over the simulation time to reduce noise. Note the units of equations (22) and (23). The advection velocity as we have defined it has units of angle per time. Thus equation (25) has units of time. An equivalent formulation could be constructed in terms of scale heights, but would introduce an additional coordinate transformation, as *vbhlight* uses approximately spherical coordinates.

We emphasize that the advection time τ_a incorporates the *total* time it takes for a fluid packet to change latitude. This includes both the “random walk” in z and the azimuthal motion of the disk orbit. The advection velocity (22) incorporates only motion in the θ direction, not the total speed of a fluid packet. Thus the increased time a packet takes to change latitude due to the fact that it is orbiting the black hole and motion is not entirely vertical is incorporated.

We will refer to τ_{\pm} and τ_a repeatedly throughout the text. We note that these quantities can also be computed more directly via an analysis of tracer particles, at the price that performing a time-dependent analysis becomes more difficult. We present a comparison between these two approaches below in section 4.8.

4.4. The Initial Transient

We now discuss phase (a). Figure 4 shows a moment very close to the initial time, at $t = 25GM_{\text{BH}}/c^3$ or ≈ 0.3 ms. Contours are for $\rho = 10^9$ and 10^{10} g/cm³. Although the initial torus is in *hydrostatic* equilibrium (which will be disrupted as the MRI develops), it is *not* in *weak* equilibrium. Figure 5 demonstrates this. We plot of τ_+/τ_- (left), the ratio of τ_-/τ_a (top right), and the ratio of τ_+/τ_a (bottom right). (Color bars are artificially saturated to enhance ease of visualization.) The fact that τ_- is much shorter than τ_+ and τ_a indicates rapid electron capture and subsequent rapid decrease in Y_e .

4.5. The Transition Phase

We now discuss phase (b). Figure 6 shows the density and electron fraction at roughly the beginning of this phase, $t = 500GM_{\text{BH}}/c^3$ or ≈ 7 ms. Figure 7 shows the time scales τ_+ , τ_- , and τ_a . As evidenced by the ratio of τ_+/τ_- , the disk is still deleptonizing, but the core of the disk has achieved very low electron fractions—as low as

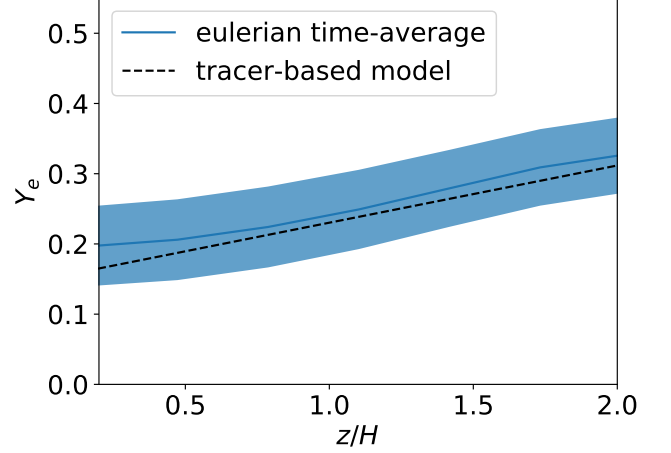


Figure 11. Vertical structure of the electron fraction, Y_e as a function of z/H , in the disk computed two ways. The solid line and envelope show the mean and standard deviation of the electron fraction averaged over the disk and over time, as computed in equations (27) and (28). The dashed line is computed using our simple 1D model (29) calibrated to tracer data.

$Y_e \sim 0.15$, similar to that in the neutron star merger disk case (Miller et al. 2019b) and consistent with Siegel et al. (2019).

At this point the relativistic, highly-magnetized jet of material characteristic of MRI-driven accretion is beginning to develop. The jet is visible as the absence of material in the polar regions in the left pane of Figure 6. In our simulation, Baryon loading from the artificial atmosphere required by the Eulerian nature of the simulation (c.f. Miller et al. 2019a) prevents the jet from reaching the very large Lorentz factors realized in Nature. However, the region is highly magnetized and the jet is powerful enough to evacuate the region.

4.6. The Importance of Absorption at Early Times

In phases (a) and (b), both neutrino absorption and emission matter for setting the electron fraction. One way of characterizing how much absorption matters is the neutrino optical depth τ . $\tau \ll 1$ implies a free-streaming limit, while $\tau \gg 1$ implies a diffusion limit (Castor 2004).⁴

Figure 8 shows both the rapid deleptonization of the disk and the mitigating effect due to absorption. We compute an effective opacity $\langle \kappa \rangle$ by measuring the number of neutrinos of each flavor and frequency absorbed by the gas *in-situ* in *vbhlight*. This amounts to integrating the frequency and flavor dependent opacity over

⁴ Note that the relative volume density of leptons in the gas also matters.

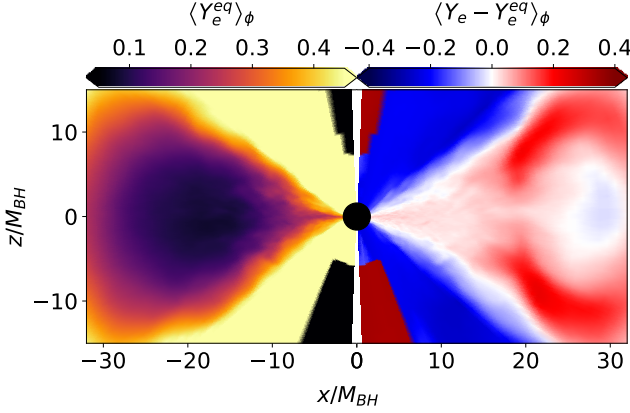


Figure 12. Equilibrium electron fraction Y_e^{eq} (left) and the difference between the true electron fraction and the equilibrium value (right) at $t = 1500 GM_{\text{BH}}/c^3$ or ≈ 22 ms and averaged over azimuthal angle ϕ . For $\sqrt{x^2 + y^2} \lesssim 20 M_{\text{BH}}$, and near the equator, the electron fraction is close to the equilibrium value. However, at higher latitudes, $Y_e^{\text{eq}} > Y_e$, driving a reionization of material as it rises in latitude.

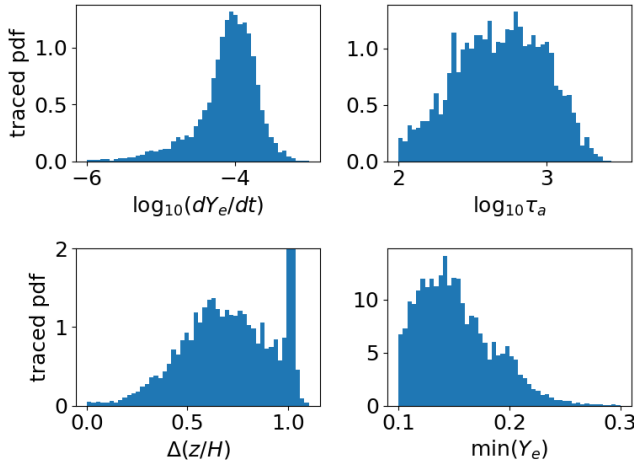


Figure 13. Probability distributions of the quantities used in equation (29) and binned from tracer particles. For this analysis, we use tracers that exist within the disk at least at time $t = 1500 GM_{\text{BH}}/c^3$ but that eventually escape.

frequency, weighted by the neutrino spectrum as realized in the simulation and summing over flavor, again weighted by the abundances per flavor as realized in the simulation. We plot this in the left pane of Figure 8. The right pane shows the co-moving derivative of electron fraction. As the disk disrupts, densities and temperatures rise near the black hole, causing opacities, and thus optical depths, to become significant, which prevents the electron fraction from dropping as rapidly.

4.7. Early-Time Quasi-Stationary Structure

We now discuss phase (c). As the accretion rate is slowly decreasing in this stage, this steady-state is not truly steady, but evolves adiabatically with time. As such we will highlight two times in this phase and describe how the system evolves adiabatically between them.

We begin with figure 9, which shows the density and electron fraction of the disk at the beginning of phase (c), roughly at $t = 1500 GM_{\text{BH}}/c^3$, or ≈ 22 ms. The jet is now well-developed, as evidenced by a sharp drop in density near the poles. Figure 10 shows time scales at the same time. At this point, the disk has finished deleptonizing. Near the equator, τ_+ and τ_- are roughly equal and shorter than τ_a , indicating the electron fraction is stable in this region.

At slightly higher latitudes, for $r \lesssim 15 GM_{\text{BH}}/c^2$, τ_+ , τ_- , and τ_a are all roughly the same order of magnitude. However, τ_+ and τ_- are out of balance, with τ_+ shorter than τ_- . We also observe that it is at this point that a stratified structure in the electron fraction begins to appear. For a given radius, Y_e is higher at higher latitudes.

We use the electron fraction averaged over radius and azimuthal angle under a change of variables from (r, θ, ϕ) to $(r, z/H, \phi)$

$$\langle Y_e \rangle_{r,\phi}(t, z/H) = \int_{r,\phi} \sqrt{-g} d^2x Y_e(t, r, z/H(r), \phi) \quad (26)$$

to define a measure of the vertical structure. We average this quantity over time in this phase to get the mean

$$\langle Y_e \rangle_{t,r,\phi}(z/H) = \frac{1}{\Delta t} \int dt \int_{r,\phi} \langle Y_e \rangle_{r,\phi}(t, z/H) \quad (27)$$

and standard deviation

$$\text{std}(Y_e)_{t,r,\phi}(z/H) = \sqrt{\frac{\int dt \left(\langle Y_e \rangle_{r,\phi} - \langle Y_e \rangle_{t,r,\phi} \right)^2}{\Delta t}} \quad (28)$$

of the vertical structure. The solid line in figure 11 shows the mean (27) and the envelope shows the standard deviation (28).

4.8. A Simple One-Dimensional Model

We propose the following simple, one-dimensional model to explain this structure. The left pane of Figure 12 shows the equilibrium electron fraction Y_e^{eq} introduced in section 4.2 at the beginning of phase (c), or $t = 1500 GM_{\text{BH}}/c^3 \approx 22$ ms. This is not the *physical* electron fraction Y_e attained in the simulation. Rather, it is the value where weak processes are in balance. The right pane shows the difference between the true Y_e and Y_e^{eq} . For $\sqrt{x^2 + y^2} \lesssim 20 M_{\text{BH}}$ and near the equator, Y_e

is close to the equilibrium value. However, at higher latitudes, $Y_e < Y_e^{\text{eq}}$.

Material at these higher latitudes is fed by material closer to the equator. As described in section 4.3, this takes time as the material “random walks” from the lower latitudes to higher latitudes.⁵ As the material rises and the density of the fluid decreases, the emission and

absorption of neutrinos raise the electron fraction. The electron fraction at a given height z relative to the scale height H is then given by the rate at which Y_e is increasing in time due to weak processes times the amount of time it took for the fluid to random walk to that height.

We use our tracer particles to implement this model as

$$Y_e(z/H) = \langle \min(Y_e) \rangle_{\text{trc}} + \left\langle \frac{dY_e}{dt} \right\rangle_{t,\text{trc}} \left(H \left\langle \frac{dz}{dt} \right\rangle_{t,\text{trc}}^{-1} \right) \left(\frac{z}{H} - \langle \min(z/H) \rangle_{\text{trc}} \right) \quad (29)$$

where we have assumed

$$\left\langle \frac{d(z/H)}{dt} \right\rangle_{t,\text{trc}}^{-1} \approx H \left\langle \frac{dz}{dt} \right\rangle_{t,\text{trc}}^{-1},$$

which is safe for slowly varying H and where

$$\langle Q \rangle_{\text{trc}} = \frac{\sum_{i=0}^{N_t} m_i Q_i}{\sum_{i=0}^{N_t} m_i} \quad (30)$$

is a mass-weighted sum over N_t tracer particles. We also define an average over tracer history:

$$\langle Q \rangle_{t,\text{trc}} = \frac{\sum_{i=0}^{N_t} m_i \int_{t_0}^{t_c} dt Q_i}{(t_c - t_0) \sum_{i=0}^{N_t} m_i}, \quad (31)$$

where t_0 is the time that the tracer achieves its minimum latitude z/H and $t_c > t_0$ is the time that the tracer then rises to a latitude of one scale height $z = H$. Here we average over tracer particles that are in the disk at $t = 1500 GM_{\text{BH}}/c^3$ but eventually become gravitationally unbound. (Here we define “gravitationally unbound” as reaching an extraction radius of $250 GM_{\text{BH}}/c^2$ with a positive Bernoulli parameter. More distant choices of extraction radius do not change the results presented here.)

The probability distributions for the parameters for equation (29) are binned from tracer particles in Figure 13. We use the mean values. Figure 11 compares our model (29) extracted from tracers to the vertical structure of Y_e in the disk extracted from an Eulerian picture of the flow. The dashed line is the 1D model fit to the tracer data and the solid line and envelope are extracted from the Eulerian picture via equations (27) and (28). The true flow structure is not entirely linear—it saturates at extreme latitudes. Nevertheless, the simple

⁵ Recall that the random walk includes not only vertical motion, but turbulent azimuthal motion as a fluid packet orbits the black hole.

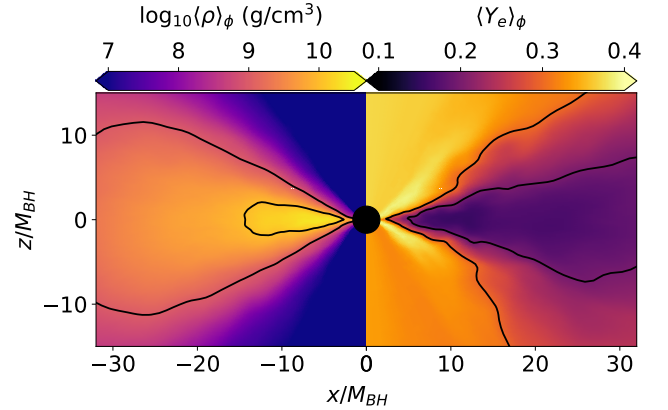


Figure 14. Same as Figure 4 but at $t = 5000 GM_{\text{BH}}/c^3$ or ≈ 73 ms.

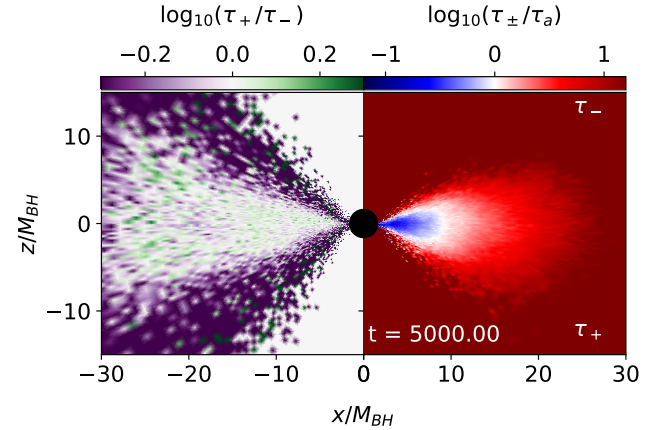


Figure 15. Same as Figure 5 but at $t = 5000 GM_{\text{BH}}/c^3$ or ≈ 73 ms.

linear model does remarkably well—agreement is well within the standard deviation.

This stratification of the electron fraction has implications in the outflow. Wind material that passes through these higher latitude regions as it leaves the disk will have its electron fraction set at least in part according

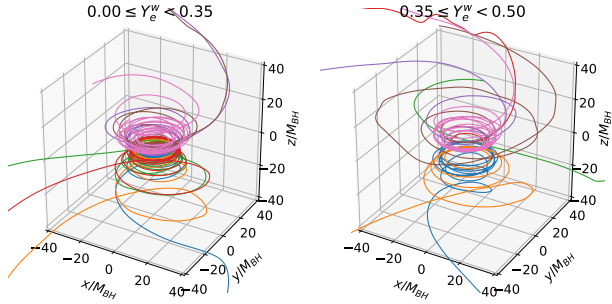


Figure 16. Paths of a selection of tracer particles in 3d. We split the tracers into those with $Y_e < 0.35$ (left) and those with $Y_e \geq 0.35$ (right). Broadly, tracers with lower electron fraction spend more time near the polar axis, while tracers with higher electron fraction spend less time. Colors highlight different traces to guide the eye.

to equation (29). Indeed, it will likely reionize further as it achieves a greater distance from the disk.

4.9. Late Times

As the disk continues to accrete, the density and accretion rate drop. Figure 14 shows the disk well into phase (c), at $t = 5000GM_{\text{BH}}/c^3$ or ≈ 73 ms. Figure 15 shows the time scales τ_+ , τ_- , and τ_a . As the density drops, the weak processes in the disk both slowly drive the disk towards larger Y_e and slowly shut off as the time scales τ_+ and τ_- gradually become large beyond dynamical relevance.

As the time scales τ_{\pm} rise, the turbulence in the disk is better able to mix the disk, and the stratified structure described in the earlier sections slowly homogenizes away. We are now in a position to understand the evolution of the mean and standard deviation of Y_e shown in figure 1. The standard deviation is a measure of stratification initially powered by weak processes and slowly erased by turbulent mixing. If we ran the simulation for longer, the accretion rate would continue to fall, the mean electron fraction would continue to rise, and the electron fraction in the disk would continue to homogenize until at very low accretion rates the disk would become composed of symmetric matter.

4.10. Outflow

We now move our attention to disk outflow and implications for nucleosynthesis. Figure 16 shows the paths of a selection of gravitationally unbound Lagrangian tracer particles. We split the tracers into those with $Y_e < 0.35$ and those with $Y_e \geq 0.35$. Qualitatively, we find that tracers with lower electron fraction tend to spend more time close to the polar axis. About 1 in 100 tracers have near-vertical trajectories, implying they may be entrained in the jet or that they are interacting with

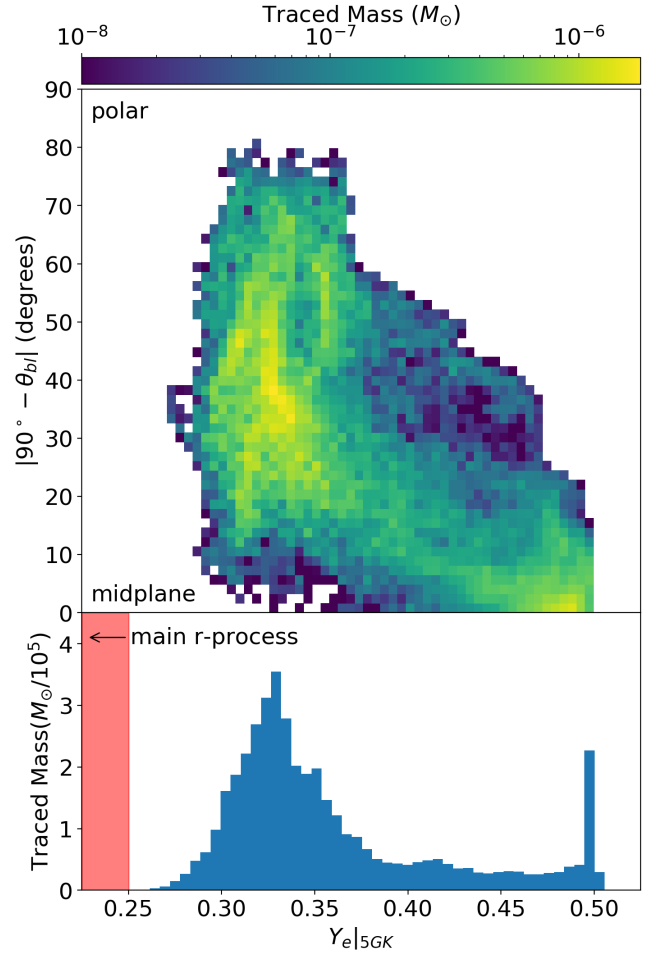


Figure 17. Electron fraction Y_e in outflow (top) vs angle and (bottom) binned by mass. The electron fraction is universally large, higher than $Y_e > 0.25$. Y_e is lower for more polar outflow. The spike in $Y_e \approx 0.5$ is from viscous spreading at the back of the disk, which never drops from its initial Y_e to low electron fraction.

the funnel wall. The prospect of nucleosynthetic material entrained in the jet has been explored in a number of works and is potentially consistent with our results. See Fujimoto et al. (2007); Ono et al. (2012); Nakamura et al. (2015); Soker & Gilkis (2017); Hayakawa & Maeda (2018) for some examples.

The electron fraction in the outflow is bounded from below by $Y_e \gtrsim 0.25$. The polar outflow has lower electron fraction than the mid-plane outflow, as shown in figure 17. This is in contrast to the neutron star merger case, where the polar outflow had *higher* electron fraction than the mid-plane (Miller et al. 2019b).

As the disk accretes, magnetically-driven turbulence transports mass in the mid-plane radially inward and angular momentum radially outward. Some material must carry this angular momentum to infinity. The outflow

driven by momentum conservation and turbulent viscosity is sometimes referred to as the viscous spreading of the disk. In the neutron star merger case, this viscous spreading is physically meaningful; the disk is not fed, but rather develops from material close to the black hole left over from the merger event. In contrast, in the jet-driven supernova case, the disk is fed by fallback material from the stellar envelope. For completeness, we record this material and count it in our analysis. However, it is not clear that mid-planar outflow will escape the star or that it is physically meaningful.

Although the electron fraction is above $Y_e \sim 0.25$, which is the approximate threshold for robust r-process nucleosynthesis, entropy can play a role in the nucleosynthetic yields as well. In particular, high entropy material may undergo robust r-process even in a less neutron-rich environment. For example, material with entropy of $s = 100 k_b/\text{baryon}$ and $Y_e = 0.35$ may undergo a robust r-process. High-velocity, shocked material entrained in the jet might become high entropy. Magnetic reconnection in the jet may also drive up entropy. Therefore, we investigate the velocity and entropy of the outflow.

Figure 18 plots the entropy and radial velocity $v_r = \partial r / \partial \tau$ (for proper time τ) of gravitationally unbound material, integrated over simulation time. The angle and radial velocity are measured at an extraction radius of $250 GM_{\text{BH}}/c^2$ or about 1000 km. At this radius, the average tracer temperature is about $2GK$. The entropy is measured when the material drops below a temperature of $5GK$. We find that most material has low entropy, around $17 k_b/\text{baryon}$, and a velocity of about $0.05c$. Both distributions have short tails, with entropies as large as $65 k_b/\text{baryon}$ and velocities as large as $0.2c$. Note that this is qualitatively different from the neutron star merger case, where both disk wind and dynamical ejecta can move at a significant fraction of the speed of light (Miller et al. 2019b). Understanding this difference will be the focus of future work.

Figure 19 compares entropy and velocity with electron fraction in the gravitationally unbound material. All material with entropy greater than $\sim 20 k_b/\text{baryon}$ has electron fraction of $Y_e \gtrsim 0.35$. Similarly, the minimum and maximum velocities converge as Y_e increases, but the distribution is overall tighter in velocity and very broad in Y_e .

4.11. Nucleosynthesis

For each of the gravitationally unbound tracer particles of Sec. 4.10, we perform nucleosynthesis calculations using the nuclear reaction network Portable Routines for Integrated nucleoSynthesis Mod-

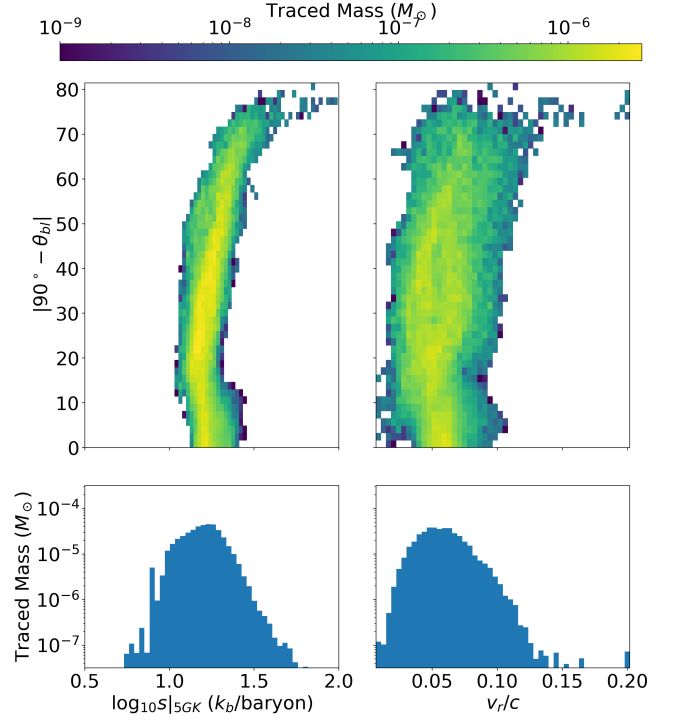


Figure 18. Histograms of entropy s (left) and velocity (right) of gravitationally unbound material. The top row compares these quantities to distance from the mid-plane $|90^\circ - \theta_{bl}|$. The bottom simply bins by mass. Most of the material is slow moving and low entropy. However, there is a short tail to the distribution, with entropies as large as $100 k_b/\text{baryon}$ and velocities as large as $0.2c$. This tail is not statistically well-resolved by the number of tracer particles we use.

eling (PRISM) (Mumpower et al. 2017; Côté et al. 2018; Zhu et al. 2018; Sprouse et al. 2019). For charged particle reaction rates, we implement the ReaLib Database (Cyburt et al. 2010). Neutron capture rates are calculated using the Los Alamos National Laboratory (LANL) statistical Hauser-Feshbach code of Kawano et al. (2016), assuming nuclear masses of FRDM2012 (Möller et al. 2012). Beta-decay properties are similarly calculated using the LANL QRPA+HF framework (Mumpower et al. 2016; Mumpower et al. 2018; Möller et al. 2019). Finally, we supplement these datasets with the nuclear decay properties of the Nubase 2016 evaluation (Audi et al. 2017) and AME2016 (Wang et al. 2017) where appropriate.

Figure 20 shows the mass-weighted nucleosynthetic yields at 1 Gyr. As expected given the electron fraction and entropy distributions, we find the outflow produces first- and (marginally) second-peak elements but no third-peak elements. Indeed, almost no elements with $A > 130$ are produced. Nucleosynthetic yields vary greatly across individual tracer particles, however the

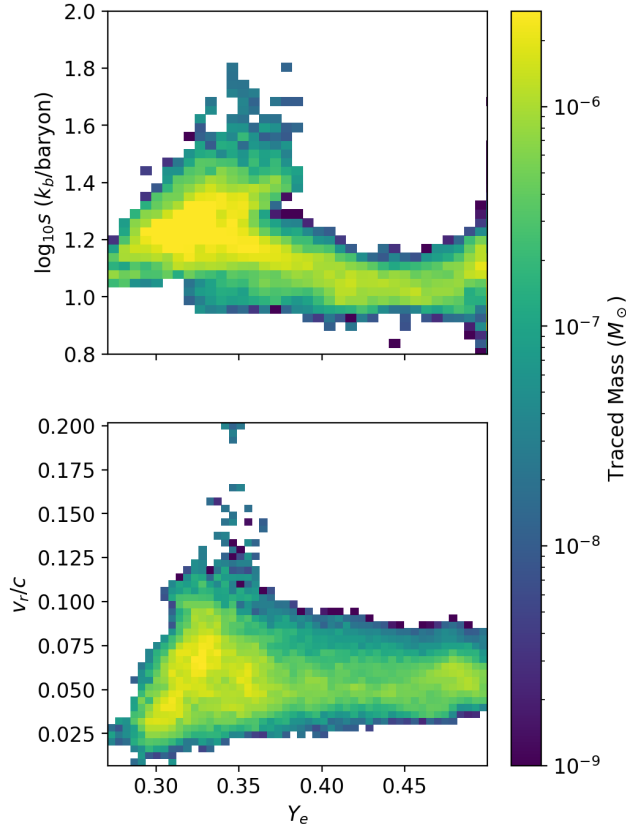


Figure 19. Histograms of entropy s (top) and velocity (bottom) vs. electron fraction Y_e for gravitationally unbound material.

overall average abundances and the lack of heavy nuclei are robust.

5. SYSTEMATICS

Following Siegel et al. (2019), our model assumes that a phase of fallback and subsequent accretion in a collapsar can be mapped to an accretion disk that has relaxed from a compact torus with $Y_e = 0.5$ in hydrostatic equilibrium (Fishbone & Moncrief 1976).⁶ (See section 3 for more details.) Here we examine this assumption.

5.1. How is Material Deleptonized?

Material in our simulation deleptonizes close to the black hole as the initial torus disrupts. In a real collapsar, material deleptonizes as it falls back onto the black hole, potentially from far away. To better understand the effects of the compact torus, we briefly investigate models that do make a more direct fallback assumption.

⁶ Note that this torus is in *hydrostatic* equilibrium. It is *not* in equilibrium with neutrino radiation field.

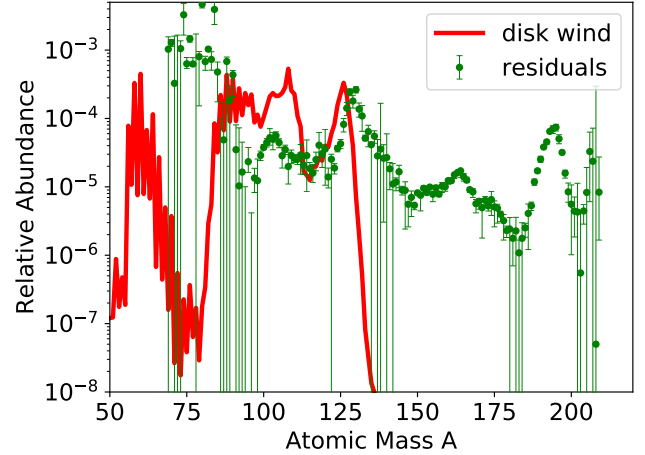


Figure 20. Mass-weighted abundances of r-process elements produced in outflow as a function of isotope mass A (red line). Green dots show r-process residuals measured from the solar system in Arnould et al. (2007). The outflow produces first and second peak r-process elements, but no third-peak. Almost no elements with $A > 130$ are produced.

We examine the model of Popham et al. (1999) and Di Matteo et al. (2002), which analytically incorporates several important neutrino emission and absorption processes and a 5-piece equation of state. These models assume a self-similar thin disk solution beginning at roughly 100km, which forms the outer boundary condition of a steady-state α model (Shakura & Sunyaev 1973). Although this model neglects much of the physics included in our simulation, the important difference in boundary conditions makes it worth discussing.

Neutrino emission and absorption rates can be estimated from the temperature and density in the disk. Surman & McLaughlin (2004) calculated the electron fraction of the disk at a given radius by balancing the time scale of deleptonization due to electron capture and subsequent neutrino emission against the time required to accrete to a given radius. Figure 21 shows the electron fraction for several analytic models computed by Surman & McLaughlin (2004). For comparison, we include the spherically averaged, density weighted electron fraction

$$\langle Y_e \rangle_{\text{SADW}}(r) = \frac{1}{t_f - t_i} \int_{t_i}^{t_f} dt \frac{\int_{S^2} Y_e \rho \sqrt{-g} d\Omega}{\int_{S^2} \rho \sqrt{-g} d\Omega} \quad (32)$$

averaged from $t_i = 5000 GM_{\text{BH}}/c^3 \approx 73$ ms to $t_f = 10^4 GM_{\text{BH}}/c^3 \approx 147$ ms from this work, where g is the determinant of the metric and the integrals are over the 2-sphere. Recall that in the case of our full three-dimensional model, we used a black hole of mass $3M_\odot$ and a dimensionless spin parameter of $a = 0.8$. Note that these averages do not reflect the diversity of physi-

cal conditions present in a simulation. They capture the location of the disk as far as it has viscously spread, but they do not show properties of, e.g., disk turbulence, the jet, or the wind. Moreover, while the work of Surman & McLaughlin (2004) assumes a time-independent solution, our system is of course time-dependent and time-averaging does a poor job of capturing this. Figure 1 shows the substantial variation in Y_e present in the simulation as a function of space and time.

Except in the innermost parts of the disk, the electron fraction of the semi-analytic disk is well above the weak equilibrium value. This is because the neutrino emission is very sensitive to the temperature and is thus simply too slow to deplete the disk before it accretes.

In the semi-analytic models, the in-falling matter is symmetric until densities and temperatures rise sufficiently, at which point electron fraction drops quickly. In contrast, we begin with a compact torus. Ideally, after sufficient time, this disk achieves a quasistationary state and “forgets” its initial conditions. However, this assumption is incompatible with the inflow-deleptonization time scale assumption in the semi-analytic models. Material in the disk has *already* deleptonized before viscously spreading outward as it reaches a steady-state. Reconciling these two pictures requires performing a full physics simulation with the correct in-fall initial and boundary conditions.

McLaughlin & Surman (2005) and Surman et al. (2006) combined the electron fraction in the disks of Surman & McLaughlin (2004) with a wind model and calculated the composition of the wind ejecta, including the effects of absorption. They found that as material leaves the disk, Y_e rises and that subsequently very little low Y_e material is ejected in their models unless the accretion rate exceeds $1 M_\odot s^{-1}$. Their analysis also relies on a balance of fluid and weak time scales, consistent with our 1D model (29) calibrated to tracer data. Although these semi-analytic models are very different from our full-physics simulation, the key result is consistent.

5.2. The Importance of Absorption for Nucleosynthesis

Although the core of the disk is low electron fraction, as described in sections 4.10 and 4.11, we find that almost none of the gravitationally unbound material is sufficiently low Y_e and high entropy to produce 3rd-peak r-process elements.

Figure 22 shows how this scenario changes if absorption is neglected, which we calculate by separately tracking changes in Y_e due to emission and absorption in our

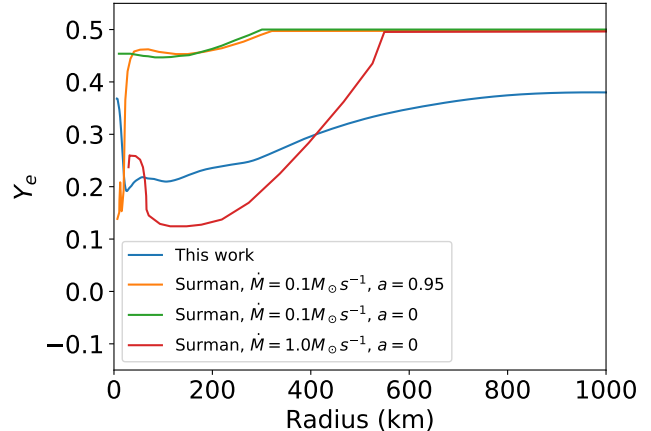


Figure 21. Electron fraction as a function of radius for several semi-analytic models, reproduced from (Surman & McLaughlin 2004). For comparison, we include the spherically averaged electron fraction computed in this work.

simulation.⁷ In the no-absorption scenario, the average electron fraction in the outflow erroneously drops from $\bar{Y}_e \approx 0.36$ to $\bar{Y}_e \approx 0.22$. This comparison implies that including absorption in these models is critical to correctly predicting nucleosynthetic yields in the outflow.

At late times, the neutrino optical depth is small, and yet we have found that treating absorption is critical to capturing the electron fraction in the outflow. As we showed in section 4.6, the physics of the early-time disk depends on the interplay between neutrino emission and absorption. Once the disk reaches a quasi-stationary state, optical depths in the disk are low—of order 10^{-3} . However, at early times, during phases (a) and (b), optical depths are of order unity.

In other words, neutrino absorption in this early phase *sets* the initial conditions of the evolution in the quasi-stationary phase (c) and thus strongly influences the electron fraction of the outflow in the steady state. For the disk to reach the *correct* steady state, absorption opacity must be accounted for.

5.3. Effect of Stellar Envelope

Section 4.10 assumes that all material with radius $r_e > 250 GM_{\text{BH}}/c^2$ and positive Bernoulli parameter is gravitationally unbound. For an accretion disk in vacuum around a black hole, this is likely a reasonable assumption. However, in a collapsar scenario, the black hole-disk system is embedded in a collapsing star. For the wind to escape, it needs not only to escape the grav-

⁷ This calculation is performed in-line in *νbhlight*. We separately record Y_e including both emission and absorption and Y_e with absorption neglected. The tracers record both quantities.

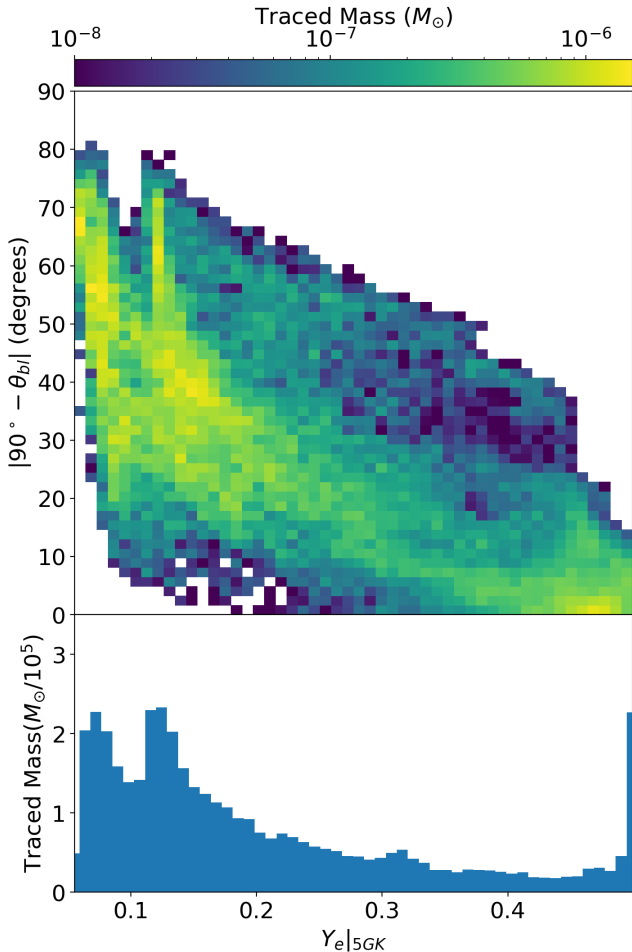


Figure 22. Electron fraction Y_e in the outflow, neglecting absorption. Top figure compares Y_e vs. angle and the bottom simply bins Y_e , weighted by tracer particle mass. In contrast to the full transport case, if absorption is neglected, the outflow contains low electron fraction material. The spike in $Y_e \approx 0.5$ is from viscous spreading at the back of the disk, which never drops to low electron fraction.

itational pull of the central black hole, but also of the star itself. Also unaccounted for is the ram pressure of in-falling material, as well as disruption of said fallback by the jet and convection and advection from the dynamics of the fallback material.

These effects, alone or together, may significantly change the amount of nucleosynthetic material which can escape the star. Understanding this requires better modeling of the disk-wind-envelope system and will be the subject of future work.

6. OUTLOOK AND IMPLICATIONS

We perform a three-dimensional general relativistic radiation magnetohydrodynamics disk simulation of a nucleosynthetically optimistic, high-accretion rate col-

lapsar disk—the first to incorporate full neutrino transport.

We find that a steady state disk forms with electron fractions near the mid-plane as low as $Y_e \sim 0.15$. At higher latitudes, however, the electron fraction is significantly larger. This quasi-steady accretion flow drives a relatively neutron-poor outflow; there is almost no unbound material produced with electron fraction less than $Y_e \sim 0.3$.

We explore the evolution of the electron fraction of the disk from the initial conditions through “late”-time quasi-stationary flow. We find the electron fraction rapidly drops as an angle dependence appears in Y_e . Over time, the electron fraction rises and homogenizes as the accretion rate drops. This drop is an artifact of the initial conditions and the fact that there is a finite reservoir of material to accrete.

We present a simple one-dimensional model explaining the dependence of the electron fraction within the flow on latitude and show that, when properly calibrated with physically meaningful parameters, the model matches the observed flow state extremely well. Although our analysis is for collapsars, it may have relevance to disks formed after neutron star mergers as well. We plan to pursue this avenue in future work.

We simulate r-process nucleosynthesis in this outflow via the PRISM reaction network (Mumpower et al. 2017; Zhu et al. 2018; Sprouse et al. 2019) and find almost no material with an atomic mass above $A \sim 130$ is produced. Our results thus imply that, even in the most nucleosynthetically optimistic case, wind-driven off of accretion disks in collapsars likely cannot act as a source for third-peak r-process elements. Indeed, since collapsars produce first- and second-peak r-process elements but not third-peak ones, including them as a significant source of light r-process elements at all may be in tension with the galactic chemical evolution and the solar abundance pattern (Côté et al. 2018).

We compare our model to the GRMHD model of Siegel et al. (2019) and the semi-analytic models developed in the literature (Popham et al. 1999; Di Matteo et al. 2002; Surman & McLaughlin 2004; McLaughlin & Surman 2005). We find the electron fraction in our disk is significantly higher than reported in Siegel et al. (2019), but lower than predicted in Surman & McLaughlin (2004); McLaughlin & Surman (2005). Moreover, we find that the electron fraction in our outflow is consistent with the semi-analytic picture.

A potential confounding factor in understanding the electron fraction in both the disk and the outflow is our use of a compact torus initial condition. This torus construction is a standard in the disk community. How-

ever, it is likely not appropriate for modeling a collapsar. First, the compact torus chosen provides a reservoir of material too close to the black hole, which means the gas does not have time to naturally deleptonize as it accretes. Second, the compact torus initial data ignores the presence of a star around and feeding the disk. If the disk is fed, the accretion rate will not drop as the power law found in this work. Rather it will depend on the mass fallback rate. Moreover, as we discussed in section 5.3, the stellar envelope may have a significant effect on the mass in the outflow.

We argue that our discrepancy with Siegel et al. (2019) is related to how the initial conditions proceed to equilibrium when absorption is or is not included. Including absorption allows us to more closely match the flow state of a collapsar, where the disk is fed by fallback.

However, an obvious improvement is to use an initial condition that reflects the reality of a collapsing star. This strategy, adopted in the early work of MacFadyen & Woosley (1999), would also allow us to better understand exactly how much ejecta escapes the star. As discussed in section 5.3, this is difficult to address in a simulation that begins with an equilibrium torus. We will pursue such a program in future work.

We conclude by emphasizing three takeaway messages from our work. First, accurate treatments of neutrino transport and neutrino absorption are required to capture the evolution of Y_e . Second, initial conditions should be carefully considered for collapsar modeling. Finally, our model supports previous conclusions that even under optimistic assumptions, wind blown off of accretion disks in collapsars cannot act as a robust source of r-process material.

7. ACKNOWLEDGEMENTS

We thank Adam Burrows, Eliot Quataert, Charles Gammie, Jim Stone, Philipp Moesta, Luke Roberts,

Benoit Cote, Sam Jones, Wes Even, Oleg Korobkin, Ryan Wollaeger, Sanjana Curtis, Greg Salvesen, and Daniel Siegel for many helpful discussions. We also thank our anonymous reviewer for challenging us to pursue a deeper analysis of the dynamics of the disk.

We acknowledge support from the U.S. Department of Energy Office of Science and the Office of Advanced Scientific Computing Research via the Scientific Discovery through Advanced Computing (SciDAC4) program and Grant DE-SC0018297

This work was supported by the US Department of Energy through the Los Alamos National Laboratory. Additional funding was provided by the Laboratory Directed Research and Development Program, the Center for Space and Earth Science (CSES), and the Center for Nonlinear Studies at Los Alamos National Laboratory under project numbers 20190021DR, 20180475DR (TS), and 20170508DR. This research used resources provided by the Los Alamos National Laboratory Institutional Computing Program. Los Alamos National Laboratory is operated by Triad National Security, LLC, for the National Nuclear Security Administration of U.S. Department of Energy under Contract No. 89233218CNA000001.

This article is cleared for unlimited release, LA-UR-19-30392.

We are grateful to the countless developers contributing to open source projects on which we relied in this work, including Python (Rossum 1995), the GNU compiler (Stallman & Developer Community 2009), numpy and scipy (van der Walt et al. 2011; Jones et al. 2001–), Matplotlib (Hunter 2007), the GNU scientific library (Galassi & Gough 2009), and HDF5 (The HDF Group 1997-2019).

REFERENCES

- Arnould, M., Goriely, S., & Takahashi, K. 2007, *Physics Reports*, 450, 97
- Audi, G., Kondev, F. G., Wang, M., Huang, W. J., & Naimi, S. 2017, *Chinese Physics C*, 41, 030001
- Balbus, S. A., & Hawley, J. F. 1991, *ApJ*, 376, 214
- Batta, A., & Lee, W. H. 2014, *MNRAS*, 437, 2412
- Blinnikov, S. I., et al. 1984, *Soviet Astronomy Letters*, 10, 177
- Bovard, L., & Rezzolla, L. 2017, *Classical and Quantum Gravity*, 34, 215005
- Bruenn, S. W. 1985, *ApJS*, 58, 771
- Bucciantini, N., Quataert, E., Arons, J., Metzger, B. D., & Thompson, T. A. 2008, *MNRAS*, 383, L25
- Burrows, A. 2018, Private correspondence, private correspondence
- Burrows, A., Reddy, S., & Thompson, T. A. 2006, *Nuclear Physics A*, 777, 356
- Castor, J. 2004, *Radiation Hydrodynamics, Radiation Hydrodynamics* (Cambridge University Press)
- Côté, B., et al. 2018, *ApJ*, 855, 99
- Cowan, J. J., Sneden, C., Lawler, J. E., et al. 2019, arXiv e-prints, arXiv:1901.01410
- Cowling, T. G. 1933, *MNRAS*, 94, 39

- Cowling, T. G. 1957, *The Quarterly Journal of Mechanics and Applied Mathematics*, 10, 129
- Cyburt, R. H., Amthor, A. M., Ferguson, R., et al. 2010, *ApJS*, 189, 240, REACLIB is available at <https://groups.nsl.msui.edu/jina/reaclib/db/>
- Di Matteo, T., Perna, R., & Narayan, R. 2002, *ApJ*, 579, 706
- Dolence, J. C., Gammie, C. F., Mościbrodzka, M., & Leung, P. K. 2009, *The Astrophysical Journal Supplement Series*, 184, 387
- Fishbone, L. G., & Moncrief, V. 1976, *ApJ*, 207, 962
- Freedman, D. Z. 1974, *Phys. Rev. D*, 9, 1389
- Fujimoto, S.-i., Hashimoto, M.-a., Kotake, K., & Yamada, S. 2007, *ApJ*, 656, 382
- Fujimoto, S.-i., Kotake, K., Yamada, S., Hashimoto, M.-a., & Sato, K. 2006, *ApJ*, 644, 1040
- Galassi, M., & Gough, B. 2009, *GNU Scientific Library: Reference Manual*, GNU manual (Network Theory)
- Galeazzi, F., Kastaun, W., Rezzolla, L., & Font, J. A. 2013, *Phys. Rev. D*, 88, 064009
- Gammie, C. F., McKinney, J. C., & Tóth, G. 2003, *The Astrophysical Journal*, 589, 444
- Ghirlanda, G., Nava, L., Ghisellini, G., Celotti, A., & Firmani, C. 2009, *A&A*, 496, 585
- Halevi, G., & Mösta, P. 2018, *MNRAS*, 477, 2366
- Hawley, J. F., Richers, S. A., Guan, X., & Krolik, J. H. 2013, *ApJ*, 772, 102
- Hayakawa, T., & Maeda, K. 2018, *ApJ*, 854, 43
- Heger, A., Fryer, C. L., Woosley, S. E., Langer, N., & Hartmann, D. H. 2003, *ApJ*, 591, 288
- Hjorth, J., & Bloom, J. S. 2012, in *Gamma-Ray Bursts*, ed. C. Kouveliotou, R. Wijers, & S. Woosley (Cambridge: Cambridge University Press, Cambridge), 169–189
- Howard, W. M., Arnett, W. D., Clayton, D. D., & Woosley, S. E. 1972, *ApJ*, 175, 201
- Hunter, J. D. 2007, *Computing In Science & Engineering*, 9, 90
- Jones, E., et al. 2001–, *SciPy: Open source scientific tools for Python*, <http://www.scipy.org/>
- Kawano, T., Capote, R., Hilaire, S., & Chau Huu-Tai, P. 2016, *Physical Review C*, 94, 014612
- Kerr, R. P. 1963, *Phys. Rev. Lett.*, 11, 237
- Kohri, K., Narayan, R., & Piran, T. 2005, *ApJ*, 629, 341
- Kumar, P., Narayan, R., & Johnson, J. L. 2008, *MNRAS*, 388, 1729
- Lattimer, J. M., Mackie, F., Ravenhall, D. G., & Schramm, D. N. 1977, *ApJ*, 213, 225
- Lattimer, J. M., & Schramm, D. N. 1976, *ApJ*, 210, 549
- Lazzati, D., Perna, R., & Begelman, M. C. 2008, *MNRAS*, 388, L15
- Lindner, C. C., Milosavljević, M., Shen, R., & Kumar, P. 2012, *ApJ*, 750, 163
- Liu, T., Gu, W.-M., & Zhang, B. 2017, *New A Rev.*, 79, 1
- López-Cámara, D., Morsony, B. J., Begelman, M. C., & Lazzati, D. 2013, *ApJ*, 767, 19
- MacFadyen, A. I., & Woosley, S. E. 1999, *The Astrophysical Journal*, 524, 262
- MacFadyen, A. I., Woosley, S. E., & Heger, A. 2001, *ApJ*, 550, 410
- McLaughlin, G. C., & Surman, R. 2005, *Nuclear Physics A*, 758, 189
- Metzger, B. D., Thompson, T. A., & Quataert, E. 2008, *ApJ*, 676, 1130
- Miller, J. M., Ryan, B. R., & Dolence, J. C. 2019a, *The Astrophysical Journal Supplement Series*, 241, 30
- Miller, J. M., Ryan, B. R., Dolence, J. C., et al. 2019b, *Phys. Rev. D*, 100, 023008
- Mizuno, Y., Yamada, S., Koide, S., & Shibata, K. 2004, *ApJ*, 606, 395
- Möller, P., Myers, W. D., Sagawa, H., & Yoshida, S. 2012, *Physical Review Letters*, 108, 052501
- Morsony, B. J., Lazzati, D., & Begelman, M. C. 2007, *ApJ*, 665, 569
- Mösta, P., Roberts, L. F., Halevi, G., et al. 2018, *ApJ*, 864, 171
- Mösta, P., Richers, S., Ott, C. D., et al. 2014, *ApJ*, 785, L29
- Mumpower, M. R., Kawano, T., & Möller, P. 2016, *Phys. Rev. C*, 94, 064317
- Mumpower, M. R., Kawano, T., Sprouse, T. M., et al. 2018, *ApJ*, 869, 14
- Mumpower, M. R., Kawano, T., Ullmann, J. L., Krťička, M., & Sprouse, T. M. 2017, *Physical Review C*, 96, doi:10.1103/PhysRevC.96.024612
- Möller, P., Mumpower, M., Kawano, T., & Myers, W. 2019, *Atomic Data and Nuclear Data Tables*, 125, 1
- Nagakura, H., Ito, H., Kiuchi, K., & Yamada, S. 2011, *ApJ*, 731, 80
- Nagataki, S., Takahashi, R., Mizuta, A., & Takiwaki, T. 2007, *ApJ*, 659, 512
- Nakamura, K., Kajino, T., Mathews, G. J., Sato, S., & Harikae, S. 2015, *A&A*, 582, A34
- O’Connor, E., & Ott, C. D. 2010a, *Classical and Quantum Gravity*, 27, 114103
- . 2010b, *Stellar Collapse: Microphysics*, online access. <https://stellarcollapse.org/equationofstate>
- Ono, M., Hashimoto, M., Fujimoto, S., Kotake, K., & Yamada, S. 2012, *Progress of Theoretical Physics*, 128, 741
- Ott, C. D., Reisswig, C., Schnetter, E., et al. 2011, *Phys. Rev. Lett.*, 106, 161103

- Popham, R., et al. 1999, *The Astrophysical Journal*, 518, 356
- Porth, O., Chatterjee, K., Narayan, R., et al. 2019, arXiv e-prints, arXiv:1904.04923
- Proga, D., MacFadyen, A. I., Armitage, P. J., & Begelman, M. C. 2003, *The Astrophysical Journal*, 599, L5
- Radice, D., et al. 2016, *Monthly Notices of the Royal Astronomical Society*, 460, 3255
- Rockefeller, G., Fryer, C. L., & Li, H. 2006, arXiv e-prints, astro
- Rockefeller, G., Fryer, C. L., Young, P., et al. 2008, arXiv e-prints, arXiv:0811.4650
- Rossum, G. 1995, *Python Reference Manual*, Tech. rep., Amsterdam, The Netherlands, The Netherlands
- Ruffert, M., et al. 1997, *A&A*, 319, 122
- Ryan, B. R., Dolence, J. C., & Gammie, C. F. 2015, *The Astrophysical Journal*, 807, 31
- Sano, T., ichiro Inutsuka, S., Turner, N. J., & Stone, J. M. 2004, *The Astrophysical Journal*, 605, 321
- Shakura, N. I., & Sunyaev, R. A. 1973, *Astronomy and Astrophysics*, 500, 33
- Shapiro, S., & Teukolsky, S. 2008, *Black Holes, White Dwarfs, and Neutron Stars: The Physics of Compact Objects* (Wiley)
- Shiokawa, H., Dolence, J. C., Gammie, C. F., & Noble, S. C. 2011, *The Astrophysical Journal*, 744, 187
- Siegel, D. M., Barnes, J., & Metzger, B. D. 2019, *Nature*, 569, 241
- Siegel, D. M., & Metzger, B. D. 2018, *The Astrophysical Journal*, 858, 52
- Skinner, M. A., Dolence, J. C., Burrows, A., Radice, D., & Vartanyan, D. 2019, *ApJS*, 241, 7
- Soker, N., & Gilkis, A. 2017, *ApJ*, 851, 95
- Sprouse, T. M., Perez, R. N., Surman, R., et al. 2019, submitted to *Physical Review*, arXiv: 1901.10337
- Stallman, R., & Developer Community. 2009, *Using the Gnu Compiler Collection: A Gnu Manual for Gcc Version 4.3.3* (SoHo Books)
- Steiner, A. W., Hempel, M., & Fischer, T. 2013, *ApJ*, 774, 17
- Surman, R., & McLaughlin, G. C. 2004, *The Astrophysical Journal*, 603, 611
- Surman, R., McLaughlin, G. C., & Hix, W. R. 2006, *The Astrophysical Journal*, 643, 1057
- Taylor, P. A., Miller, J. C., & Podsiadlowski, P. 2011, *MNRAS*, 410, 2385
- The HDF Group. 1997-2019, *Hierarchical Data Format*, version 5, <http://www.hdfgroup.org/HDF5/>
- Thompson, T. A., Chang, P., & Quataert, E. 2004, *ApJ*, 611, 380
- Uzdensky, D. A., & MacFadyen, A. I. 2007, *ApJ*, 669, 546
- van der Walt, S., Colbert, S. C., & Varoquaux, G. 2011, *Computing in Science Engineering*, 13, 22
- Wang, M., Audi, G., Kondev, F. G., et al. 2017, *Chinese Phys. C*, 41, 030003
- Winteler, C., Käppeli, R., Perego, A., et al. 2012, *ApJ*, 750, L22
- Woosley, S. E. 1993, *ApJ*, 405, 273
- Woosley, S. E., & Bloom, J. S. 2006, *ARA&A*, 44, 507
- Zhu, Y., Wollaeger, R. T., Vassh, N., et al. 2018, *The Astrophysical Journal*, 863, L23